

# Thin film growth and mechanical properties of CrFeCoNi/TiNbZrTa multilayers

Smita G. Rao<sup>a,\*</sup>, Rui Shu<sup>a</sup>, Siyang Wang<sup>b</sup>, Robert Boyd<sup>a</sup>, Finn Giuliani<sup>b</sup>, Arnaud le Febvrier<sup>a</sup>, Per Eklund<sup>a</sup>

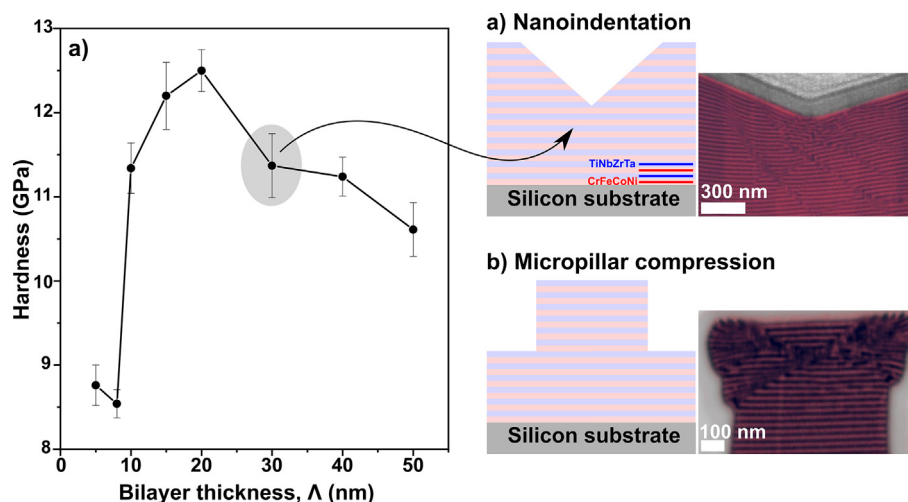
<sup>a</sup> Department of Physics, Chemistry, and Biology (IFM), Linköping University, Linköping 58183, Sweden

<sup>b</sup> Department of Materials, Faculty of Engineering, Imperial College London, London SW7 2AZ, United Kingdom

## HIGHLIGHTS

- High entropy alloy-based CrFeCoNi/TiNbZrTa multilayer thin films grown by direct current (dc)-magnetron sputtering.
- Multilayer structure analysis by X-ray diffraction and transmission electron microscopy.
- Mechanical property characterization by nanoindentation and micropillar compression.

## GRAPHICAL ABSTRACT



## ARTICLE INFO

### Article history:

Received 1 July 2022

Revised 17 October 2022

Accepted 17 November 2022

Available online 18 November 2022

### Keywords:

High entropy alloy  
Multilayers  
Mechanical properties  
Compression

## ABSTRACT

Multilayers of high entropy alloys (HEA) are picking up interest due to the possibility of altering material properties by tuning crystallinity, thickness, and interfaces of the layers. This study investigates the growth mechanism and mechanical properties of CrFeCoNi/TiNbZrTa multilayers grown by magnetron sputtering. Multilayers of bilayer thickness ( $\Lambda$ ) from 5 nm to 50 nm were grown on Si(100) substrates. Images taken by transmission electron microscopy and energy-dispersive X-ray spectroscopy mapping revealed that the layers were well defined with no occurrence of elemental mixing. Multilayers with  $\Lambda < 20$  nm exhibited an amorphous structure. As  $\Lambda$  increased, the CrFeCoNi layer displayed a higher crystallinity in comparison to the amorphous TiNbZrTa layer. The mechanical properties were influenced by the crystallinity of the layers and stresses in the film. The film with  $\Lambda = 20$  nm had the highest hardness of approximately 12.5 GPa owing to grain refinement of the CrFeCoNi layer. An increase of  $\Lambda \geq 30$  nm resulted in a drop in the hardness due to the increase in crystal domains of the CrFeCoNi layer. Micropillar compression induced shear in the material rather than fracture, along with elemental intermixing in the core of the deformed region of the compressed micropillar.

© 2022 The Authors. Published by Elsevier Ltd. This is an open access article under the CC BY license (<http://creativecommons.org/licenses/by/4.0/>).

\* Corresponding author.

E-mail address: [smita.gangaprasad.rao@liu.se](mailto:smita.gangaprasad.rao@liu.se) (S.G. Rao).

## 1. Introduction

The trend in metallic materials research has shifted from binary and ternary alloys to high entropy alloys (HEA), which are materials where each alloying element is present in equal to near equal ratios. The concept which is no longer unfamiliar in materials science research was introduced in 2004 with the discovery of the Cantor alloy (CrMnFeCoNi) and introduction of the term “high entropy alloy” [1,2]. The realm of HEA-based materials has since then quickly expanded from the metallic Cantor alloy system to refractory metal-based alloys along with high entropy alloy-based ceramics and metallic glasses [3,4]. These materials are now finding application in the industry sector because of their exceptional mechanical, electrochemical and thermal properties [5–7]. More recently, the field of HEA-based multilayers and superlattices are starting to gain popularity.

Superlattices were first studied in the 1980s to understand dislocation dynamics at nitride interfaces and the effects of strained layers. The initial studies were carried out on TiN/VN and TiN/NbN superlattices grown on MgO (100) wafers by dc magnetron sputtering. It was found that the films exhibited an increased hardness which may be a result of a decrease in the mobility of dislocations due to the strained super lattices [8–10]. Since then, nanostructured multilayers and superlattices have been widely studied due to their impressive mechanical properties, tribological properties, thermal stability, radiation tolerance, and also optical properties [11–14]. The goal now is to make use of HEA based materials to further improve on the existing multilayer systems. In regard to this, studies on NbMoTaW/CoCrNi multilayers grown by dc-magnetron sputtering have showed that the main mechanism for material strengthening was through the obstruction of dislocation movement at grain boundaries and interfaces [15]. On the other hand (AlCrTiZrV)/SiC multilayers deposited with varying SiC thickness showed that crystallization and epitaxial like growth of the SiC layer on the AlCrTiZrV layer was believed to have a strengthening effect on the film [16]. Studies on AlCrMoNbZr/(AlCrMoNbZr)N multilayers grown by magnetron sputtering showed that the individual layer thickness determined the interface stability which in turn influenced the mechanical and properties of the films [17].

We see that the strengthening mechanism in each multilayer system is highly dependent on the HEA-based material chosen. What we require is a fundamental understanding of the influence of the bilayer thickness, crystallinity, and stresses on the mechanical properties of these complex structured systems starting with traditional systems such as the face center cubic (fcc) Cantor alloy and the body centered cubic (bcc) refractory HEA. Therefore, in this study we investigate the growth mechanism along with the mechanical properties when alternating layers of two representative multicomponent systems: CrFeCoNi and TiNbZrTa.

## 2. Experimental details

CrFeCoNi/TiNbZrTa multilayered thin films were grown with bilayer thicknesses ( $\Lambda$ ) ranging from 5 nm to 50 nm on Si(100) substrates at room temperature by magnetron sputtering using compound targets (Cr<sub>24</sub>Fe<sub>32</sub>Co<sub>24</sub>Ni<sub>20</sub> and Ti<sub>25</sub>Nb<sub>25</sub>Zr<sub>25</sub>Ta<sub>25</sub> provided by Plansee, Composite Materials GmbH, 2-inch diameter). Prior to deposition, the substrates were cleaned with acetone and isopropanol for 10 min each in an ultrasonic bath and blow-dried with nitrogen gas. The deposition system was evacuated to a base pressure  $<9 \times 10^{-7}$  Pa. The Ar pressure was fixed at 0.53 Pa (4.0 mTorr). A detailed description of the deposition system can be found in reference [18]. Both the compound targets were sputtered

by setting the dc power at 100 W. The bilayer thickness was controlled by varying the deposition time of the individual targets. The volumetric fraction of the layers was kept constant at 50 %. All the multilayers had a total film thickness of  $\sim 500$  nm. The multilayer with  $\Lambda = 30$  nm was also grown with a total film thickness of  $\sim 2 \mu\text{m}$  for nanopillar compression study. In addition to the multilayer series, single bilayers with total thickness lower  $<100$  nm were grown for X-ray reflectivity (XRR) measurements along with 500 nm thick monolithic reference films of CrFeCoNi and TiNbZrTa under the same deposition conditions. The composition of films was nearly identical to these targets as confirmed by Energy Dispersive X-Ray Spectroscopy (EDS) and provided in the supplementary information (Table S1).

X-ray diffraction techniques (XRD) were used to analyze the crystal structure, residual stress, and thickness of the multilayers. The instruments were operated using Cu-K $\alpha$  radiation ( $\lambda = 1.54056 \text{ \AA}$ ) at a voltage of 45 kV and current of 40 mA regardless of the technique being used. A PANalytical X'Pert PRO diffractometer in Bragg-Brentano setup was used to obtain diffractograms to identify the crystal structure. Residual stress and thickness were obtained from the measurements carried out using a PANalytical Empyrean X-ray diffractometer. The residual stress was calculated by measuring the curvature of the substrate from the offset in  $\omega$  of the peak of a certain symmetrical reflection (Si 006 at  $69.3^\circ$ ) while the sample was moved in x and y. The Stoney equation was used to calculate the average stresses from the curvature of the Si(100) substrate [19]. The thickness of the bilayers was estimated from XRR measurements (Supplementary Fig. S1).

Nanoindentation measurements were carried out in displacement-control mode using Hysitron Triboindenter 950 equipped with a 2D transducer. The instrument was calibrated along the indentation axis using a standard fused silica reference. A set of 20 indents were made on each sample using a Berkovich tip. The maximum load was set at 1.5  $\mu\text{N}$  for all the 500 nm thick films in order to maintain the indentation depth at 10 % of the total film thickness. The hardness (H) and reduced elastic modulus ( $E_r$ ) of the films were calculated according to the Oliver-Pharr method [20].

For the micropillar compression test, circular micropillars of 2  $\mu\text{m}$  in height and  $\sim 3$  in aspect ratio were fabricated using Ga focused ion beam (FIB) milling on a FEI Helios 5 Dualbeam microscope. Thermo Scientific NanoBuilder software was used to set up the FIB patterning profile. The acceleration voltage of the FIB was set to 30 kV and a series of FIB beam currents from 2.1 nA down to 40 pA were used. A High current beam was used to produce a 20  $\mu\text{m}$ -diameter trench around the micropillar in order to achieve *in situ* visualization of the micropillar during the compression tests, while low current beam was used for the final tailoring of the micropillar contour as per [21–23]. *In situ* scanning electron microscope (SEM) micropillar compression tests were carried out using a displacement-controlled Alemnis nanoindenter, on a FEI Quanta 650 SEM. A 5  $\mu\text{m}$ -diameter circular flat punch indenter was used in order to achieve a uniaxial stress state. A loading speed of 5 nm/s was applied.

FIB milling was used to prepare the cross-section specimens from the micropillars and indents for observation with SEM, and to lift out thin foils for transmission electron microscopy (TEM) analysis. A Zeiss Neon 40 dual beam workstation using 30 kV/2nA Ga $^+$  ion was used to prepare electron transparent TEM thin foil specimens. These thin foils were extracted by the lift-out technique. A final thinning down and polishing was carried out using 200 pA and 50 pA currents. (Scanning) TEM analysis of the thin foil specimens was performed using a FEI Tecnai G2 TF 20 UT instrument operated at 200 kV, in order to observe the layered structure and the deformation in the layers.

### 3. Results

#### 3.1. X-Ray diffraction

Fig. 1 presents the  $\theta$ -2 $\theta$  XRD pattern obtained from CrFeCoNi/TiNbZrTa multilayer films with varied  $\Lambda$  from 5 to 50 nm, along with the monolithic reference CrFeCoNi and TiNbZrTa films. Si substrate peaks are observed at  $2\theta$  values of  $32.9^\circ$  (002 forbidden reflection) and  $69.3^\circ$  (004 reflection). The monolithic reference films are crystalline in nature with the TiNbZrTa film preferentially orientated along the [110] of a bcc structure ( $a = 3.39 \pm 0.02$  Å) and the CrFeCoNi film preferentially oriented along the [111] of an fcc structure ( $a = 3.56 \pm 0.02$  Å). The multilayered films are shown in shades of green with the  $\Lambda$  indicated to the left of the XRD patterns. The film with the  $\Lambda = 5$  nm shows low intensity broad peaks indicating that both layers have low levels of crystallinity or small crystal domains (X-ray amorphous). As  $\Lambda$  is increased to 20 nm (CrFeCoNi layer of 10 nm) the peak intensity of the fcc-CrFeCoNi (111) reflection (Peaks at approximately at  $2\theta = 44.1^\circ$ ) increases in intensity indicating the growth of crystalline domains. The peak corresponding to the bcc (110) at  $2\theta = 37.6^\circ$  of the TiNbZrTa layer remains to be low in intensity and therefore can be considered to be X-ray amorphous. The films with  $\Lambda = 30, 40$  and  $50$  nm display Pendellosung fringes near the (111) peak of CrFeCoNi [24]. This is an indication of smooth interfaces or small surface roughness between the layers and is commonly seen in superlattices [25,26]. In summary, the crystallinity of the CrFeCoNi layers is greater for  $\Lambda$  from 20 to 50 nm, while the TiNbZrTa layers remained amorphous with low diffracted intensities.

#### 3.2. Mechanical properties

Fig. 2a shows the hardness evolution measured by nanoindentation as a function of the bilayer thickness  $\Lambda$ . Since all the films had an approximate thickness of 500 nm, the depths of the indents were maintained at 10 % of the film thickness by carrying out the indents with a maximum load of 1.5  $\mu$ N. The reference monolithic films of TiNbZrTa and CrFeCoNi both show similar hardness values of approximately 10.5 GPa. The multilayers with  $\Lambda$  of 5 and 10 nm have an approximate hardness of 8.5 GPa, which is lower than the monolithic reference films. Note here that the reference monolithic films have different states of crystallinity as observed by XRD

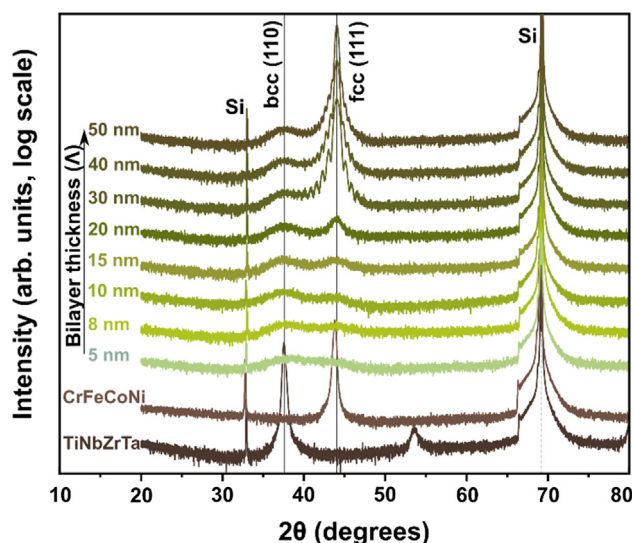


Fig. 1. 0-2 $\theta$  X-ray diffractograms obtained from CrFeCoNi/TiNbZrTa multilayered films with increasing  $\Lambda$ .

where thin layer were found to be X-ray amorphous. As the modulation period is increased, the maximum hardness is observed for a  $\Lambda = 10$  nm until 30 nm after which the hardness drops, and the films exhibit similar hardness as the monolithic films. The reduced Young's modulus is seen to increase up to a  $\Lambda$  of 40 nm after which it drops from  $\sim 225$  GPa to  $\sim 195$  GPa. Note that, as  $\Lambda$  increases, the number of layers the indenter passes through decreases. Therefore, for the multilayer with  $\Lambda = 50$  nm, the indenter passes through two layers with the topmost layer being TiNbZrTa and the second layer being CrFeCoNi.

Fig. 2c shows the residual stress values in the films. The monolithic references exhibit similar stress levels but different types. The TiNbZrTa film exhibits compressive stresses ( $\sim -0.65$  GPa) while the CrFeCoNi film has tensile stress ( $\sim 0.65$  GPa). The multilayers with  $\Lambda \leq 20$  nm have relatively similar compressive residual stress around  $-0.5$  GPa. As the  $\Lambda$  increases, the compressive stress is suppressed. The film with  $\Lambda = 30$  nm is seen to be completely stress free. Further increase of  $\Lambda$  results to tensile stresses at around  $+0.1$  GPa.

Fig. 2d shows the top-view SEM image of an indent with a depth of  $\sim 200$  nm carried out on the film with  $\Lambda = 30$  nm and total film thickness of 2  $\mu$ m. The hardness of this 2  $\mu$ m thick film was found to be on par with the hardness of the 500 nm thick film ( $\sim 10$  GPa) while the modulus was slightly lower ( $\sim 175$  GPa). The profile of the indent shows no signs of cracks however a pile up of materials can be observed. To further analyze the indent and understand the behavior of this multilayer film, TEM samples were made from the area marked in the yellow rectangle in Fig. 2d. Fig. 2e shows the cross-section TEM images of the indent where the slip bands are seen to propagate through the whole film. A closer look at the area directly beneath the indenter tip is seen in Fig. 2f. The layered structure is maintained even close to the surface; however, it can be observed that most of the slip bands are concentrated at the top 300–400 nm of the surface and propagates at a  $45^\circ$  angle with respect to the loading axis.

Based on the results obtained from XRD and nanoindentation, it was observed that the multilayer with  $\Lambda = 30$  nm displayed the most interesting behavior (crystallinity, free of or low residual stress, good hardness and young modulus) and therefore was chosen for further micropillar compression tests.

#### 3.3. Micropillar compression

Fig. 3 shows the SEM images of the micropillars prior (Fig. 3a) and post (Fig. 3c and d) compression testing with a nominal engineering strain corresponding to 10 and 20 % of the micropillar height respectively. Tapering of the pillars will lead to concentrated plastic flow near the top as can be observed in Fig. 3 (c,d). Although this unlikely affects the yield stresses measured, readers should note that the hardening rates on Fig. 3 (b) could vary if the size and shape of test pieces are changed. Nominal engineering stress and strain were calculated by dividing load with mid-height cross sectional area of the micropillar and dividing displacement with the height of the micropillar, respectively. A maximum engineering stress of 4.5 GPa for a 20 % nominal engineering strain was observed (Fig. 3b).

Fig. 4a and 4b show the TEM images, inset SAED pattern and EDS maps of the CrFeCoNi/TiNbZrTa multilayer film with  $\Lambda = 30$  nm. The cross-section image of the nanopillar displays a well-defined layered structure (Fig. 4b). A closer inspection of the layers high resolution (HR)TEM, (Fig. 4c) shows that the CrFeCoNi layer is crystalline while the TiNbZrTa layer is found to be amorphous. From the inset SAED pattern in Fig. 4b, the bright spots correspond to reflections from the fcc-structured CrFeCoNi layer. The lattice parameter was calculated to be  $3.55 \pm 0.04$  Å, comparable to that of the Cantor alloy which has a lattice parameter of  $\sim 3.6$  Å [1].



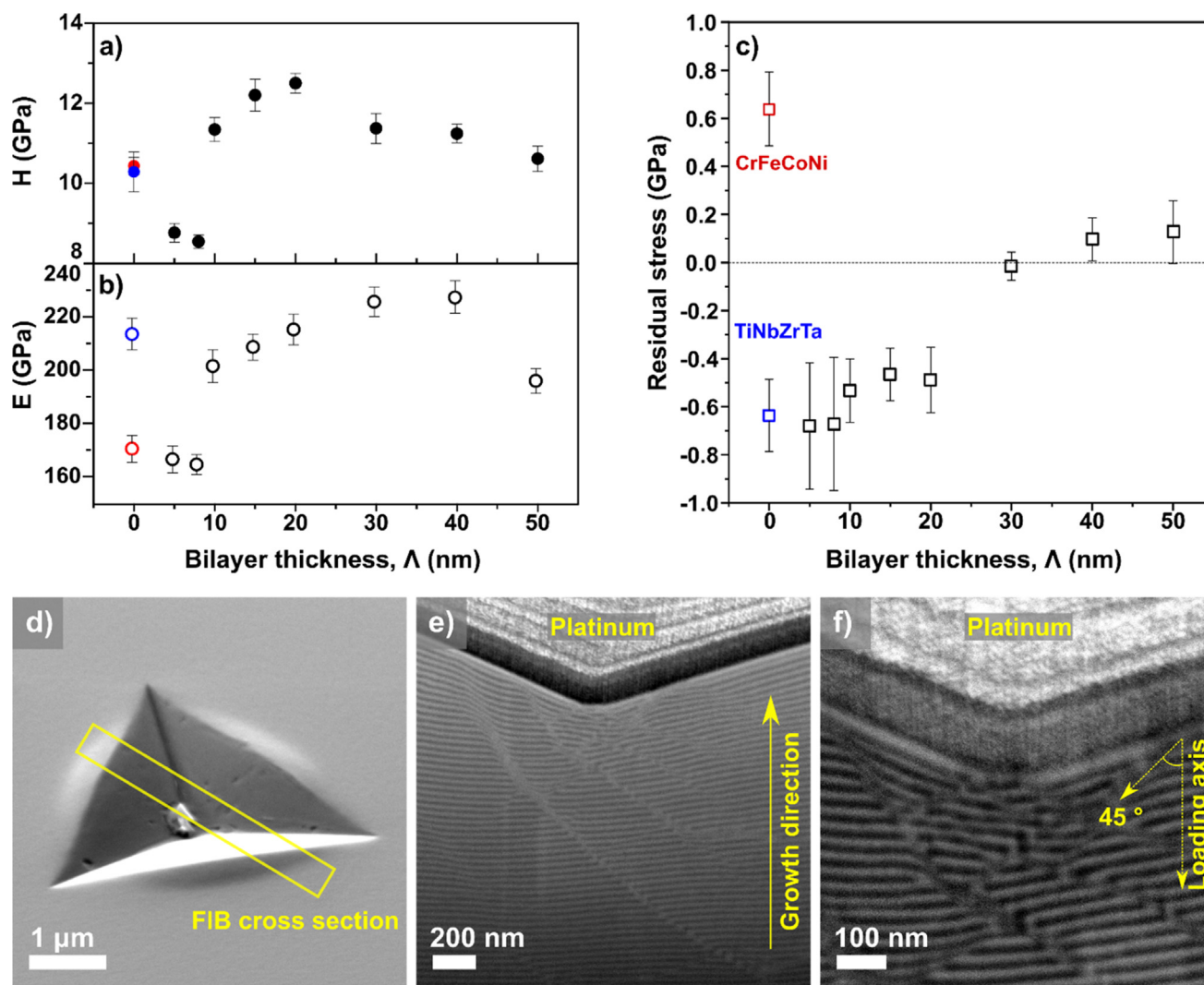


**Fig. 2.** (a) Hardness( $H$ ) and (b) reduced Young's modulus ( $E_r$ ) of multilayered films and (c) Residual stress measured of multilayered films obtained from XRD. Values marked in blue indicate the hardness, modulus, and stress values of the monolithic reference TiNbZrTa film while values marked in red indicate the same for the monolithic reference CrFeCoNi film (d) top-view SEM image of indentation imprint on the film with  $\Lambda = 30$  nm. Rectangle in yellow marks the area where the FIB lamella was taken from for TEM analysis. (e) and (f) are cross-section SEM images indicating the shear bands within the film.

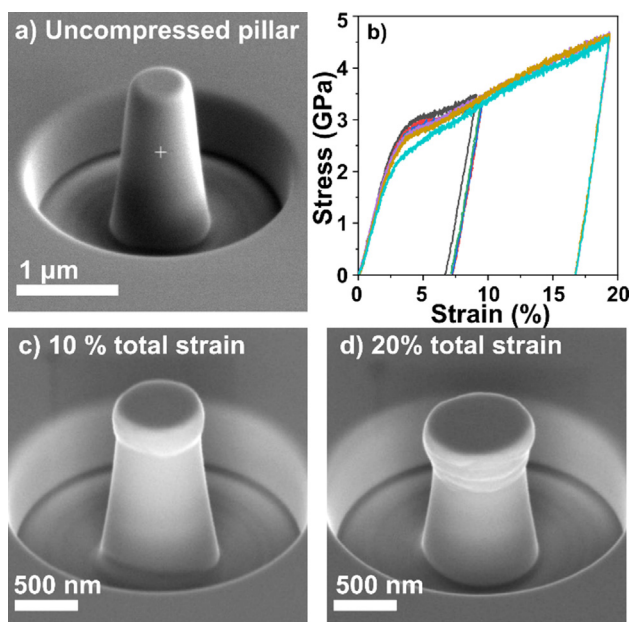
The results obtained from TEM corroborate well with those of XRD. The EDS maps (Fig. 2b) taken from the same cross-sectional area indicate that no observed intermetallic segregation or diffusion occurred between the layers.

Fig. 4d shows the STEM cross-section image of the micropillar compressed with 20 % nominal engineering strain. The plastic deformation caused by the applied load was restricted to the top 400 nm, after which the multilayers remained intact. Shear bands in the shape of a “X” can be observed in the same 400 nm region, however no fracture is observed. A closer look at the layers in this 400 nm region reveals that the CrFeCoNi layer is able to retain its structure while the TiNbZrTa layer is more prone to deformation (arrows in Fig. 4d), resulting in squeeze out effect and a mushroom shape. HRTEM images taken from three regions, (i) above the deformed region, (ii) at the maximum deformation zone and (iii) below the deformed region, are shown in Fig. 4d (i), 4d (ii), and 4d (iii), respectively. The layered structure along with the crystallinity of the CrFeCoNi layer remains intact directly above and below the deformed region (Fig. 4i and iii). In the maximum deformation zone, the layered structure is disrupted, and the elements of each layer intermix resulting in an amorphous-like structure (Fig. 4d ii).

#### 4. Discussion

Differences in terms of crystallinity were observed in the two material systems when combined to form multilayers. The CrFeCoNi layer became highly crystalline when  $\Lambda \geq 30$  nm. While the TiNbZrTa layer remained X-ray amorphous even when  $\Lambda$  exceeded 30 nm (Fig. 1). The [111] preferred orientation growth and crystallization of CrFeCoNi is due to the fact that the (111) plane of the fcc structure has the highest packing density and therefore the lowest surface energy [27]. This allows for the growth and crystallization of CrFeCoNi grains even at lower thicknesses ( $\Lambda \geq 20$  nm). On the other hand, TiNbZrTa layer crystallized with a bcc structure with a [110] preferred orientation observed on the monolithic coating. This plane has a higher surface energy in comparison to the fcc (111) and therefore would require higher energy to nucleate [27]. Moreover, the atoms in the (110) plane would not be able to accommodate themselves on the CrFeCoNi fcc [111] oriented grains, which could be the reason for the formation of the X-ray amorphous layer even when  $\Lambda > 20$  nm.

The stress in the multilayered films predominantly depend on  $\Lambda$  and the crystallinity of the two materials in the film. In the early stage of film growth ( $\Lambda < 20$  nm), the islands in either of the layers



**Fig. 3.** (a) SEM image of micropillar produced by FIB. (b) Stress vs strain curves corresponding to (c) and (d), SEM images of micropillars post compression testing with 10 % and 20 % nominal engineering strain respectively.

are in the stage of precoalescence and are therefore subject to capillary forces [28,29]. These forces result in overall compressive stress in the multilayer. As the bilayer thickness increases, the time for the islands to coalesce increases and grain boundaries are formed. This would result in a decrease in the compressive stresses and eventually lead to a tensile stressed material [30]. Similar turnaround behavior has been observed in Ni films grown by magnetron sputtering, where the stress evolves as the grain size increases during growth [31]. This type of stress evolution from compressive to tensile and back to compressive (CTC) is common in materials grown on weakly interacting substrates [28].

The mechanical properties of coatings and multilayer are dependent on the stress and the crystallinity of the film. Based on the crystallinity of the multilayers we can group the films into three categories, the amorphous/amorphous multilayers ( $\Lambda = 5\text{--}8\text{ nm}$ ) which exhibit compressive stresses, the nanocrystalline/amorphous multilayers ( $\Lambda = 10\text{--}20\text{ nm}$ ) which also exhibit compressive stresses, and the crystalline/amorphous multilayers ( $\Lambda = 30\text{--}50\text{ nm}$ ) which are stress free to tensile stressed. At this point the readers are advised to be cautious in their interpretation of the hardness and modulus results and focus on the general trends.

At the low  $\Lambda$  values (5 and 8 nm), in the stages of precoalescence when both layers exhibit a metallic-glass-like structure, the films have high low hardness. The absence of grain boundaries and lack of atomic order allows for localized shear deformation. Since the hardness of a material is determined by its ability to inhibit shear band motion, these films display the lowest hardness.

In the case of the nanocrystalline/amorphous multilayers, as the CrFeCoNi layer starts to form small crystal domains ( $\Lambda = 10\text{--}20\text{ nm}$ ) with the same compressive stress the hardness increases which is therefore a result of grain refinement in the CrFeCoNi layer along with the amorphous TiNbZrTa layer which inhibits the movement of dislocations from the crystalline CrFeCoNi layer [32].

For the crystalline/amorphous multilayers the CrFeCoNi layer is well crystallized. As the thickness of the CrFeCoNi increases the crystal domains increase in size (Fig. 1). This would allow dislocations to glide with ease along the length of the crystal domain and

therefor result in a drop in the hardness. The tensile stresses do not contribute to improving the mechanical properties of the multilayers. Similar trends of an initial increase in hardness and eventual drop as bilayer thickness increases have been observed in multiple studies [33–35].

Studies on CrMnFeCoNi/TiZrNbHfTa multilayers of two different  $\Lambda$  (5 and 50 nm) were carried out by Jiang *et al.* [36]. Their study showed that the film with the amorphous/amorphous layer ( $\Lambda = 5\text{ nm}$ ) had a higher hardness (7.8 GPa) in comparison to the amorphous/crystalline layers ( $\Lambda = 50\text{ nm}$ ) which displayed a hardness of 5.6 GPa. The higher hardness in the  $\Lambda = 5\text{ nm}$  film was argued to be a result of the amorphous nature and the material inability to propagate plastic strain [36]. The present study shows similar range of hardness values as reported by Jiang *et al.* while also providing a more detailed picture on the evolution of stress, mechanical properties and crystallinity in HEA multilayered systems. Even though a drop in the hardness is observed with increasing  $\Lambda$  it may be more likely due to the tensile stress and not the degree of crystallinity in the layers. A graph of the multilayer hardness plotted as a function of the residual stresses can be found in the supplementary information (Fig. S2).

Mechanical testing not only leads to the apparent deformation of the multilayer but can also induce intermixing between the layers. Atomistic imaging along with molecular dynamic simulation of TiN/AlN interfaces have shown that nanoindentation can cause intermixing of the two materials to form a solid solution of  $\text{Ti}_{1-x}\text{Al}_x\text{N}$  due to a rise in interfacial energy resulting from an accumulation of interface dislocations [37]. Fig. 2 shows post indentation TEM images of the stress-free film ( $\Lambda = 30\text{ nm}$ ) where the effect of intermixing is not observed between the layers. The majority of the shear bands are concentrated at the surface and are at a  $45^\circ$  angle to the loading axis. Intermixing of elements is however observed in the compressed micropillar (Fig. 4). Here the mixing that occurs in the core of the deformed region is due to the plastic deformation and strain localization. Similar “mechanical alloying” effect have been observed in other studies on crystalline/amorphous multilayers where elements from the crystalline layer can intermix into the amorphous layer via dislocations and shear of the crystallites [38,39].

## 5. Conclusion

CrFeCoNi/TiNbZrTa multilayers of varying  $\Lambda$  (5–50 nm) were grown on Si(100) substrates by magnetron sputtering. At lower  $\Lambda$  the CrFeCoNi layer was found to be amorphous but gradually crystallized in a fcc structure as  $\Lambda$  increased. The TiZrNbTa layer on the other hand remained amorphous regardless of the  $\Lambda$ . The hardness of the films obtained from nanoindentation depended on  $\Lambda$  which in turn depended on the crystallinity of the film. The highest hardness of approximately 12.5 GPa was seen for the multilayer with  $\Lambda = 20\text{ nm}$ . This was largely due to grain refinement in the CrFeCoNi layer. Micropillar compression measurements showed no traces of fracture. STEM cross-sectional images indicated that the TiZrNbTa layer had a larger extent of deformation in comparison to the CrFeCoNi layer. The results for the study indicate that the HEA multilayered films can be strengthened by tuning the bilayer thickness and the crystallinity of the individual layers.

## 6. Data availability statement

Data are available from the corresponding author on reasonable request.



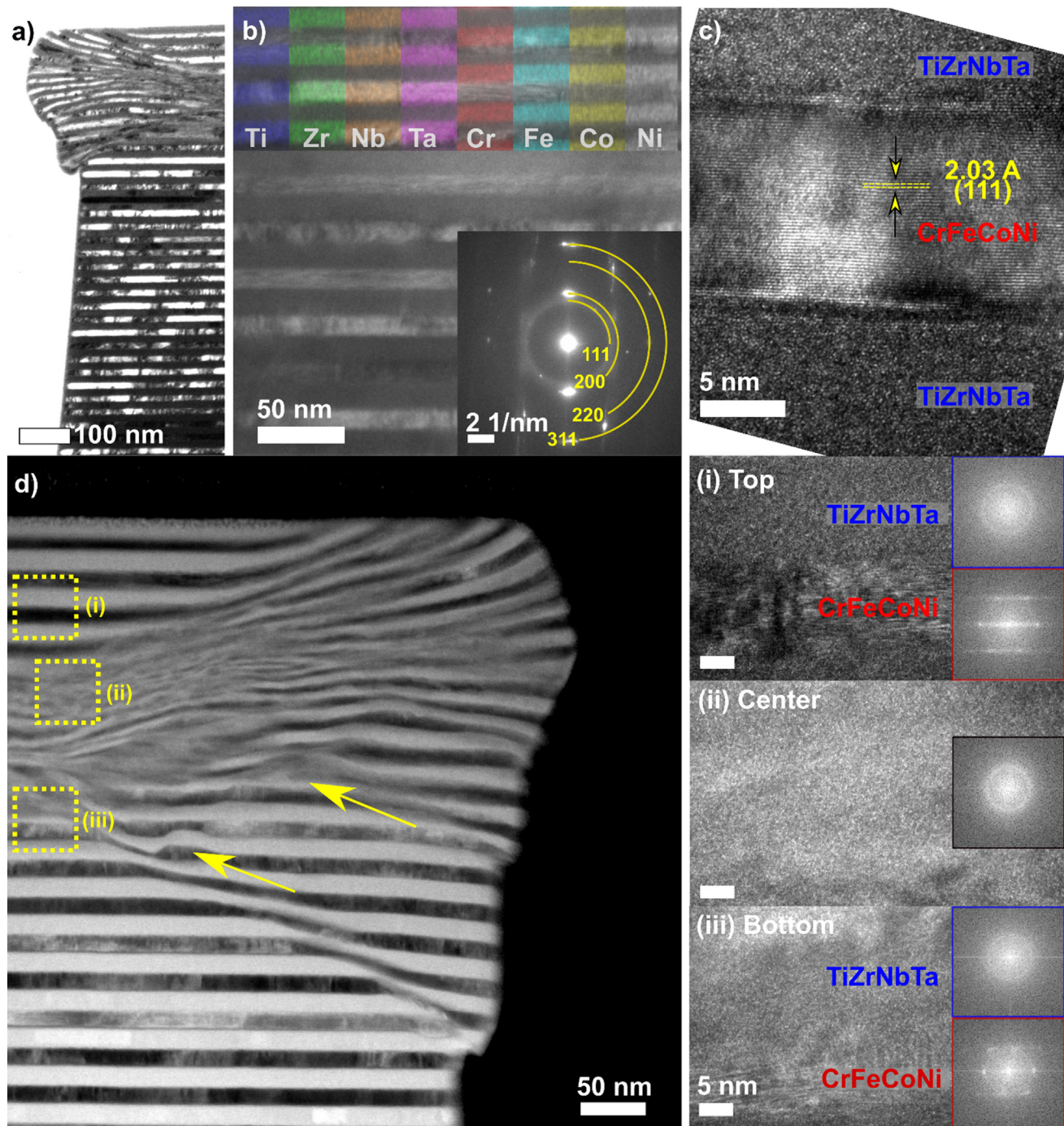


**Fig. 4.** (a) TEM image of  $\Lambda = 30$  nm films after compression testing showing distinct layers. (b) zoomed in TEM image of uncompressed region with inset SAED pattern taken from bulk of uncompressed film cross-section. Corresponding elemental EDS maps are shown on the top. (c) High resolution (HR)TEM image from uncompressed region. (d) STEM image of deformed region along with corresponding HRTEM images of zones marked (i), (ii) and (iii).

#### Data availability

Data will be made available on request.

#### Declaration of Competing Interest

The authors declare that they have no known competing financial interests or personal relationships that could have appeared to influence the work reported in this paper.

#### Acknowledgments

This work was supported financially by the VINNOVA Competence Centre FunMat-II (grant no. 2016-05156), the Swedish Government Strategic Research Area in Materials Science on Functional Materials at Linköping University (Faculty Grant SFO-Mat-LiU No. 2009 00971), the Knut and Alice Wallenberg foundation through the Wallenberg Academy Fellows program (KAW-2020.0196) and the Swedish Research Council (VR) under project number 2021-03826.

## References

- [1] B. Cantor, I.T.H. Chang, P. Knight, A.J.B. Vincent, Microstructural development in equiatomic multicomponent alloys, *Mater. Sci. Eng. A* 375–377 (2004) 213–218, <https://doi.org/10.1016/j.msea.2003.10.257>.
- [2] J.W. Yeh, S.K. Chen, S.J. Lin, J.Y. Gan, T.S. Chin, T.T. Shun, C.H. Tsau, S.Y. Chang, Nanostructured high-entropy alloys with multiple principal elements: Novel alloy design concepts and outcomes, *Adv. Eng. Mater.* 6 (2004) 299–303, <https://doi.org/10.1002/adem.200300567>.
- [3] D.B. Miracle, O.N. Senkov, A critical review of high entropy alloys and related concepts, *Acta Mater.* 122 (2017) 448–511, <https://doi.org/10.1016/j.actamat.2016.08.081>.
- [4] E.P. George, D. Raabe, R.O. Ritchie, High-entropy alloys, *Nat. Rev. Mater.* 4 (2019) 515–534, <https://doi.org/10.1038/s41578-019-0121-4>.
- [5] C. Oses, C. Toher, S. Curtarolo, High-entropy ceramics, *Nat. Rev. Mater.* 5 (2020) 295–309, <https://doi.org/10.1038/s41578-019-0170-8>.
- [6] X. Yan, Y. Zhang, Functional properties and promising applications of high entropy alloys, *Scr. Mater.* 187 (2020) 188–193, <https://doi.org/10.1016/j.SCRMAT.2020.06.017>.
- [7] E.J. Pickering, A.W. Carruthers, P.J. Barron, S.C. Middleburgh, D.E.J. Armstrong, A.S. Gandy, High-entropy alloys for advanced nuclear applications, *Entropy* 23 (2021) 98, <<https://doi.org/10.3390/E23010098>>.
- [8] U. Helmersson, S. Todorova, S.A. Barnett, J.-E. Sundgren, L.C. Markert, J.E. Greene, Growth of single-crystal TiN/VN strained layer superlattices with extremely high mechanical hardness, *J. Appl. Phys.* 62 (2) (1987) 481–484.
- [9] M. Shinn, L. Hultman, S.A. Barnett, Growth, structure, and microhardness of epitaxial TiN/NbN superlattices, *J. Mater. Res.* 7 (1992) 901–911, <https://doi.org/10.1557/JMR.1992.0901>.
- [10] E. Bauer, J.H. van der Merwe, Structure and growth of crystalline superlattices: from monolayer to superlattice, *Phys. Rev. B* 33 (6) (1986) 3657–3671.
- [11] S. Zheng, I.J. Beyerlein, J.S. Carpenter, K. Kang, J. Wang, W. Han, N.A. Mara, High-strength and thermally stable bulk nanolayered composites due to twin-induced interfaces, *Nat. Commun.* 13 (2022) 1–8, <<https://doi.org/10.1038/ncomms2651>>.
- [12] M.M. Primorac, M.D. Abad, P. Hosemann, M. Kreuzeder, V. Maier, D. Kiener, Elevated temperature mechanical properties of novel ultra-fine grained Cu–Nb composites, *Mater. Sci. Eng. A* 625 (2015) 296–302, <https://doi.org/10.1016/j.msea.2014.12.020>.
- [13] J. Wang, R. Shu, J. Chai, S.G. Rao, A. le Febvrier, H. Wu, Y. Zhu, C. Yao, L. Luo, W. Li, P. Gao, P. Eklund, Xe ion irradiation-induced structural transitions and elemental diffusion in high-entropy alloy and nitride thin-film multilayers, *SSRN Electron. J.* (2022), <https://doi.org/10.2139/SSRN.3992160>.
- [14] N. Koutná, L. Löfler, D. Holec, Z. Chen, Z. Zhang, L. Hultman, P.H. Mayrhofer, D. G. Sangiovanni, Atomistic mechanisms underlying plasticity and crack growth in ceramics: a case study of AlN/TiN superlattices, *Acta Mater.* 229 (2022), <https://doi.org/10.1016/j.actamat.2022.117809> 117809.
- [15] Z.H. Cao, Y.J. Ma, Y.P. Cai, G.J. Wang, X.K. Meng, High strength dual-phase high entropy alloys with a tunable nanolayer thickness, *Scr. Mater.* 173 (2019) 149–153, <https://doi.org/10.1016/j.SCRMAT.2019.08.018>.
- [16] B. Li, X. Ma, W. Li, Q. Zhai, P. Liu, K. Zhang, F. Ma, J. Wang, Effect of SiC thickness on microstructure and mechanical properties of (AlCrTiZrV)N/SiC nanomultilayers film synthesized by reactive magnetron sputtering, *Thin Solid Films* 730 (2021) 138724, <<https://doi.org/10.1016/j.tsf.2021.138724>>.
- [17] W. Zhang, R. Tang, Z.B. Yang, C.H. Liu, H. Chang, J.J. Yang, J.L. Liao, Y.Y. Yang, N. Liu, Preparation, structure, and properties of high-entropy alloy multilayer coatings for nuclear fuel cladding: a case study of AlCrMoNbZr/(AlCrMoNbZr)N, *J. Nucl. Mater.* 512 (2018) 15–24, <https://doi.org/10.1016/j.jnucmat.2018.10.001>.
- [18] A. le Febvrier, L. Landälv, T. Liersch, D. Sandmark, P. Sandström, P. Eklund, An upgraded ultra-high vacuum magnetron-sputtering system for high-velocity and software-controlled deposition, *Vacuum* 187 (2021) 110137.
- [19] G.C.A.M. Janssen, M.M. Abdalla, F. van Keulen, B.R. Pujada, B. van Venrooy, Celebrating the 100th anniversary of the Stoney equation for film stress: developments from polycrystalline steel strips to single crystal silicon wafers, *Thin Solid Films* 517 (2009) 1858–1867, <https://doi.org/10.1016/j.tsf.2008.07.014>.
- [20] W.C. Oliver, G.M. Pharr, Measurement of hardness and elastic modulus by instrumented indentation: advances in understanding and refinements to methodology, *J. Mater. Res.* 19 (2004) 3–20, <https://doi.org/10.1557/jmr.2004.19.1.3>.
- [21] S. Wang, F. Giuliani, T. Ben Britton, Variable temperature micropillar compression to reveal <a> basal slip properties of Zircaloy-4, *Scr. Mater.* 162 (2019) 451–455, <https://doi.org/10.1016/j.SCRMAT.2018.12.014>.
- [22] S. Wang, F. Giuliani, T. Ben Britton, Slip–hydride interactions in Zircaloy-4: multiscale mechanical testing and characterisation, *Acta Mater.* 200 (2020) 537–550, <https://doi.org/10.1016/j.actamat.2020.09.038>.
- [23] S. Wang, O. Gavalda-Diaz, T. Luo, L. Guo, E. Lovell, N. Wilson, B. Gault, M.P. Ryan, F. Giuliani, The effect of hydrogen on the multiscale mechanical behaviour of a La(Fe, Mn, Si)13-based magnetocaloric material, *J. Alloys Compd.* 906 (2022), <https://doi.org/10.1016/j.jallcom.2022.164274> 164274.
- [24] V.I. Punegov, X-ray Laue diffraction by sectioned multilayers. I. Pendellösung effect and rocking curves, *J. Synchrotron Radiat.* 28 (2021) 1466–1475, <https://doi.org/10.1107/S1600577521006408>.
- [25] C. Kim, S.B. Qadri, M.R. Scanlon, R.C. Cammarata, Low-dimension structural properties and microindentation studies of ion-beam-sputtered multilayers of Ag/Al films, *Thin Solid Films* 240 (1994) 52–55, [https://doi.org/10.1016/0040-6090\(94\)90692-0](https://doi.org/10.1016/0040-6090(94)90692-0).
- [26] A.T. Macrander, K.E. Strege, X-ray double-crystal characterization of highly perfect InGaAs/InP grown by vapor-phase epitaxy, *J. Appl. Phys.* 59 (2) (1986) 442–446.
- [27] S.G. Wang, E.K. Tian, C.W. Lung, Surface energy of arbitrary crystal plane of bcc and fcc metals, *J. Phys. Chem. Solids* 61 (2000) 1295–1300, [https://doi.org/10.1016/S0022-3697\(99\)00415-1](https://doi.org/10.1016/S0022-3697(99)00415-1).
- [28] G. Abadias, E. Chason, J. Keckes, M. Sebastiani, G.B. Thompson, E. Barthel, G.L. Doll, C.E. Murray, C.H. Stoessel, L. Martinu, Review Article: Stress in thin films and coatings: Current status, challenges, and prospects, *J. Vac. Sci. Technol. A Vacuum, Surfaces, Film* 36 (2) (2018) 020801.
- [29] C. Friesen, C.V. Thompson, R. Koch, D. Hu, A.K. Das, Comment on “compressive stress in polycrystalline volmer-weber films”, *Phys. Rev. Lett.* 95 (2005), <https://doi.org/10.1103/PhysRevLett.95.229601> 146101.
- [30] W.D. Nix, B.M. Clemens, Crystallite coalescence: A mechanism for intrinsic tensile stresses in thin films, *J. Mater. Res.* 14 (1999) 3467–3473, <https://doi.org/10.1557/JMR.1999.0468>.
- [31] H.Z. Yu, C.V. Thompson, Grain growth and complex stress evolution during Volmer-Weber growth of polycrystalline thin films, *Acta Mater.* 67 (2014) 189–198, <https://doi.org/10.1016/j.actamat.2013.12.031>.
- [32] M. Zhang, B. Yang, J. Chu, T.G. Nieh, Hardness enhancement in nanocrystalline tantalum thin films, *Scr. Mater.* 54 (2006) 1227–1230, <https://doi.org/10.1016/j.SCRMAT.2005.12.027>.
- [33] T.G. Nieh, J. Wadsworth, High strength freestanding metal-amorphous multilayers, *Scr. Mater.* 44 (2001) 1825–1830, [https://doi.org/10.1016/S1359-6462\(01\)00801-6](https://doi.org/10.1016/S1359-6462(01)00801-6).
- [34] M.C. Liu, J.C. Huang, H.S. Chou, Y.H. Lai, C.J. Lee, T.G. Nieh, A nanoscaled underlayer confinement approach for achieving extraordinarily plastic amorphous thin film, *Scr. Mater.* 61 (2009) 840–843, <https://doi.org/10.1016/j.SCRMAT.2009.07.010>.
- [35] Y. Wang, J. Li, A.V. Hamza, T.W. Barbee, Ductile crystalline-amorphous nanolaminates, *Proc. Natl. Acad. Sci. U. S. A.* 104 (2007) 11155–11160, [https://doi.org/10.1073/PNAS.0702344104/SUPPL\\_FILE/IMAGE1127.GIF](https://doi.org/10.1073/PNAS.0702344104/SUPPL_FILE/IMAGE1127.GIF).
- [36] L. Jiang, Z. Bai, M. Powers, Y. Fan, W. Zhang, E.P. George, A. Misra, Deformation mechanisms in crystalline-amorphous high-entropy composite multilayers, *Mater. Sci. Eng. A* 848 (2022), <https://doi.org/10.1016/j.msea.2022.143144> 143144.
- [37] Z. Chen, Y. Zheng, L. Löfler, M. Bartosik, G.K. Nayak, O. Renk, D. Holec, P.H. Mayrhofer, Z. Zhang, Atomic insights on intermixing of nanoscale nitride multilayer triggered by nanoindentation, *Acta Mater.* 214 (2021), <https://doi.org/10.1016/j.actamat.2021.117004> 117004.
- [38] G. Wu, C. Liu, A. Brognara, M. Ghidelli, Y. Bao, S. Liu, X. Wu, W. Xia, H. Zhao, J. Rao, D. Ponge, V. Devulapalli, W. Lu, G. Dehm, D. Raabe, Z. Li, Symbiotic crystal-glass alloys via dynamic chemical partitioning, *Mater. Today* 51 (2021) 6–14, <https://doi.org/10.1016/j.mattod.2021.10.025>.
- [39] W. Guo, E.A. Jägle, P.P. Choi, J. Yao, A. Kostka, J.M. Schneider, D. Raabe, Shear-induced mixing governs codeformation of crystalline-amorphous nanolaminates, *Phys. Rev. Lett.* 113 (2014), <https://doi.org/10.1103/PHYSREVLETT.113.035501/FIGURES/4/MEDIUM> 035501.